



Deposited via The University of Leeds.

White Rose Research Online URL for this paper:

<https://eprints.whiterose.ac.uk/id/eprint/217679/>

Version: Accepted Version

---

**Article:**

Qi, G., Davies, T.E., Nasrallah, A. et al. (2022) Au-ZSM-5 catalyses the selective oxidation of CH<sub>4</sub> to CH<sub>3</sub>OH and CH<sub>3</sub>COOH using O<sub>2</sub>. *Nature Catalysis*, 5. pp. 45-54. ISSN: 2520-1158

<https://doi.org/10.1038/s41929-021-00725-8>

---

© The Author(s), under exclusive licence to Springer Nature Limited 2022. This version of the article has been accepted for publication, after peer review (when applicable) and is subject to Springer Nature's AM terms of use (<https://www.springernature.com/gp/open-research/policies/accepted-manuscript-terms>), but is not the Version of Record and does not reflect post-acceptance improvements, or any corrections. The Version of Record is available online at: <https://doi.org/10.1038/s41929-021-00725-8>.

**Reuse**

Items deposited in White Rose Research Online are protected by copyright, with all rights reserved unless indicated otherwise. They may be downloaded and/or printed for private study, or other acts as permitted by national copyright laws. The publisher or other rights holders may allow further reproduction and re-use of the full text version. This is indicated by the licence information on the White Rose Research Online record for the item.

**Takedown**

If you consider content in White Rose Research Online to be in breach of UK law, please notify us by emailing [eprints@whiterose.ac.uk](mailto:eprints@whiterose.ac.uk) including the URL of the record and the reason for the withdrawal request.

1  
2

## 1. Extended Data

Figure #	Figure title One sentence only	Filename This should be the name the file is saved as when it is uploaded to our system. Please include the file extension. i.e.: <i>Smith_ED_Fig1.jpg</i>	Figure Legend If you are citing a reference for the first time in these legends, please include all new references in the main text Methods References section, and carry on the numbering from the main References section of the paper. If your paper does not have a Methods section, include all new references at the end of the main Reference list.
----------	-----------------------------------	--	---

3  
4

## 2. Supplementary Information:

5

### A. Flat Files

Item	Present?	Filename This should be the name the file is saved as when it is uploaded to our system, and should include the file extension. The extension must be .pdf	A brief, numerical description of file contents. i.e.: <i>Supplementary Figures 1-4, Supplementary Discussion, and Supplementary Tables 1-4.</i>
Supplementary Information	Yes	Supplementary Information. pdf	Supplementary Notes 1-2, Supplementary Figures 1-25, and Supplementary Tables 1-15, Supplementary References
Reporting Summary	No		
Peer Review Information	No	<i>OFFICE USE ONLY</i>	

6

### B. Additional Supplementary Files

Type	Number If there are multiple files of the same type this should be the numerical indicator. i.e. "1" for Video 1, "2" for Video 2, etc.	Filename This should be the name the file is saved as when it is uploaded to our system, and should include the file extension. i.e.: <i>Smith_Supplementary_Video_1.mov</i>	Legend or Descriptive Caption Describe the contents of the file
------	--	--	--

7

8 **3. Source Data**

Parent Figure or Table	Filename This should be the name the file is saved as when it is uploaded to our system, and should include the file extension. i.e.: <i>Smith_SourceData_Fig1.xls</i> , or <i>Smith_Unmodified_Gels_Fig1.pdf</i>	Data description i.e.: Unprocessed Western Blots and/or gels, Statistical Source Data, etc.
Source Data Fig. 1	WH_Source_Data_Fig1	Statistical Source Data
Source Data Fig. 2	WH_Source_Data_Fig2	Statistical Source Data
Source Data Fig. 5	WH_Source_Data_Fig5	Statistical Source Data

9 **Au/ZSM-5 catalyses the selective oxidation of CH<sub>4</sub> to CH<sub>3</sub>OH and**  
10 **CH<sub>3</sub>COOH using O<sub>2</sub>**

11 Guodong Qi<sup>1</sup>, Thomas E. Davies<sup>2</sup>, Ali Nasrallah<sup>2</sup>, Mala A. Sainna<sup>2</sup>, Alexander G. R. Howe<sup>3</sup>,  
12 Richard J. Lewis<sup>2</sup>, Matthew Quesne<sup>2</sup>, C. Richard A. Catlow<sup>2</sup>, David J. Willock<sup>2</sup>, Qian He<sup>3</sup>,  
13 Donald Bethell<sup>2</sup>, Mark J. Howard<sup>2</sup>, Barry A. Murrer<sup>2</sup>, Brian Harrison<sup>2</sup>, Christopher J. Kiely<sup>4</sup>,  
14 Xingling Zhao<sup>1</sup>, Feng Deng<sup>1</sup>, Jun Xu<sup>1\*</sup> and Graham J. Hutchings<sup>2\*</sup>

15  
16 <sup>1</sup>National Centre for Magnetic Resonance in Wuhan, State Key Laboratory of Magnetic  
17 Resonance and Atomic and Molecular Physics, Innovation Academy for Precision  
18 Measurement Science and Technology, Chinese Academy of Sciences, Wuhan 430071,  
19 China. University of Chinese Academy of Sciences, Beijing 100049, China

20 <sup>2</sup> Max Planck–Cardiff Centre on the Fundamentals of Heterogeneous Catalysis FUNCAT,  
21 Cardiff Catalysis Institute, School of Chemistry, Cardiff University, Main Building, Park  
22 Place, Cardiff, CF10 3AT, UK.

23 <sup>3</sup> National University of Singapore, Singapore 117575, Singapore

24 <sup>4</sup> Department of Materials Science and Engineering, Lehigh University, 5 East Packer  
25 Avenue, Bethlehem, Pennsylvania, PA 18015, USA.

26  
27 \*[Hutch@cardiff.ac.uk](mailto:Hutch@cardiff.ac.uk); [xujun@wipm.ac.cn](mailto:xujun@wipm.ac.cn)

28

29 **Abstract**

30 The oxidation of methane, the main component of natural gas, to selectively form oxygenated  
31 chemical feedstocks using molecular oxygen has been a long-standing grand challenge in  
32 catalysis. Here, using gold nanoparticles supported on the zeolite ZSM-5 we introduce a  
33 method to oxidise methane to methanol and acetic acid in water at temperatures between 120-  
34 240 °C using molecular oxygen in the absence of any added co-reductant. Electron  
35 microscopy reveals that the catalyst does not contain gold atoms or clusters, but rather gold  
36 nanoparticles are the active component while a mechanism involving surface adsorbed  
37 species is proposed in which methanol and acetic acid are formed via parallel pathways.

38

39

40

41

## 42 Introduction

43 The direct selective oxidation of CH<sub>4</sub> to chemical intermediates using molecular oxygen is  
44 challenging since over-oxidation by combustion to CO<sub>2</sub> and H<sub>2</sub>O is thermodynamically  
45 preferred. Commercially, CH<sub>4</sub> is converted into chemicals using an indirect route involving  
46 the production of synthesis gas (CO + H<sub>2</sub>)<sup>1</sup>. However, the direct route has been the subject of  
47 intense interest for many decades<sup>2,3</sup>. Early studies focused on using gas phase reactions at  
48 moderate temperatures (400-500 °C) and oxygenated products can be observed if the  
49 temperature and the O<sub>2</sub> partial pressure are carefully controlled<sup>4</sup>. There have been many  
50 approaches to this challenge where the emphasis has been on using lower temperature to  
51 enable improved selectivity to oxygenated products, but often these involve catalytic cycles  
52 that are not closed. For example, Periana and co-workers reported that electrophilic Hg and  
53 Pt-complexes can oxidise methane in oleum<sup>5,6</sup>, forming methyl hydrogen sulfate which has to  
54 be hydrolyzed separately to release methanol and SO<sub>2</sub>.

55 Most recent interest has centred on metal-exchanged zeolite catalysts. Fe-ZSM-5 was shown  
56 to form CH<sub>3</sub>OH with N<sub>2</sub>O as oxidant<sup>7-10</sup>, FeCu-ZSM-5 forms CH<sub>3</sub>OH in high selectivity  
57 using H<sub>2</sub>O<sub>2</sub> as oxidant<sup>11,12</sup>, Cu-mordenite<sup>13</sup> and Rh-ZSM-5<sup>14,15</sup> both can form CH<sub>3</sub>OH with O<sub>2</sub>  
58 using CO as a co-reductant. Nanoparticulate AuPd alloys supported on ZSM-5 are also active  
59 with in situ formed H<sub>2</sub>O<sub>2</sub><sup>16</sup> and unsupported AuPd alloys are active with H<sub>2</sub>O<sub>2</sub><sup>17</sup>. For all these  
60 catalysts no selective oxygenate products are formed with O<sub>2</sub> alone. A detailed comparison of  
61 recently reported catalysts is presented in Supplementary Tables 1 and 2.

62 Cu-mordenite catalysts when operated in a two stage non-closed catalytic cycle can form  
63 CH<sub>3</sub>OH<sup>18-20</sup>. An oxidised Cu species is reacted with CH<sub>4</sub> to form a surface methoxyl which is  
64 subsequently extracted at a lower temperature with water. van Bokhoven and co-workers  
65 demonstrated<sup>21</sup> that Cu-mordenite can oxidise CH<sub>4</sub> with a continuous flow of H<sub>2</sub>O to produce  
66 methanol; however, this reaction is stoichiometric rather than catalytic as the turnover is 0.21  
67 mol CH<sub>3</sub>OH/mol Cu. Román-Leshkov and co-workers<sup>22,23</sup> have shown that Cu-H-ZSM-5 can  
68 oxidise methane in a continuous flow of H<sub>2</sub>O and O<sub>2</sub> and can achieve a closed catalytic cycle  
69 with low conversion and the turnover number (TON) is 1.4 after a long reaction time of 288  
70 h. Most recently Koishybay and Shantz<sup>24</sup> have shown that for methane oxidation catalysed  
71 with Cu-SSZ-13 under similar reaction conditions H<sub>2</sub>O is the source of the oxygen in the  
72 CH<sub>3</sub>OH product, but the yields are still very low. There is therefore a need to identify  
73 improved catalysts for the methane oxidation reaction.

74 Here we report that the oxidation of CH<sub>4</sub> using O<sub>2</sub> can be achieved in the absence of a co-  
75 reductant (H<sub>2</sub> or CO) in a closed catalytic cycle using Au supported on ZSM-5 with high  
76 selectivity to oxygenated products at 120-240 °C and with low CO<sub>2</sub> production.

77

## 78 **Results**

### 79 **Catalyst preparation and methane oxidation using Au/ZSM-5**

80 We prepared Au catalysts supported on ZSM-5 using a deposition precipitation method. The  
81 characterised catalysts (Supplementary Figs 1, 2 and Supplementary Table 3) were used for  
82 the direct oxidation of CH<sub>4</sub> with O<sub>2</sub> in water for 2 h at 240 °C with 3.5 bar O<sub>2</sub> and 20.7 bar  
83 CH<sub>4</sub> charged at room temperature (Table 1). It was observed that oxygenated products could  
84 be formed, in contrast to earlier studies where the presence of a co-reductant was necessary<sup>14</sup>.  
85 Under these conditions, methanol, methyl hydroperoxide, acetic acid and peracetic acid were  
86 detected using quantitative nuclear magnetic resonance (NMR) analysis (Supplementary Figs  
87 3 and 4)<sup>16,17</sup>. Significantly, there was no <sup>1</sup>H NMR evidence of formaldehyde (hydrate), its  
88 methyl hemiacetal, or of formic acid among the liquid products (Supplementary Fig. 3). The  
89 optimum final pH used in the deposition precipitation for catalyst preparation was determined  
90 to be pH 6-8 (Supplementary Figure 5) and, in all following experiments, catalysts were  
91 prepared at pH 6. We contrasted the use of ZSM-5 as a support for Au, with that of silica and  
92 alumina (Table 1 - entries 2-4, Supplementary Fig. 6). Au-ZSM-5 showed the best activity  
93 while H-ZSM-5 itself showed much lower activity and selectivity in the absence of Au (Table  
94 1 - entry 1, Supplementary Table 4) despite the presence of Fe in the zeolite samples  
95 (Supplementary Table 3).

96 The Si/Al ratio of the ZSM-5 was found to affect the catalytic performance indicating the  
97 acidity of the support is of importance. ZSM-5 was sourced from two commercial suppliers  
98 both giving similar results (Supplementary Table 5). The highest productivity was obtained  
99 with the ZSM-5 material having the lowest Si/Al ratio (23). The topology of the structure also  
100 appears to be important; Zeolite Y with a very low Si/Al ratio of 2.8 is less effective than any  
101 ZSM-5 support and a MOR material with a very similar Si/Al ratio has only half the  
102 productivity value. This is consistent with the relative proton mobility in these materials  
103 which follows the order H-ZSM-5 > H-MOR > H-Y.<sup>Error! Reference source not found.</sup> Au loading  
104 was investigated (Supplementary Figure 7) and the yield of oxygenated products increased  
105 with the amount of Au present. Furthermore, X-ray photoelectron spectroscopy showed that  
106 all catalysts contain largely Au<sup>0</sup> with some cationic Au possibly present at very low Au  
107 loading (Supplementary Figure 2). The effect of O<sub>2</sub> partial pressure was also investigated

108 (Fig. 1a-d). For low O<sub>2</sub> partial pressures the formation of the selective oxygenated products  
109 was noted with low CO<sub>2</sub> generation (Table 1, entries 4,5,7). Use of short reaction times  
110 (Figure 1e-h) showed that the over-oxidation to CO<sub>2</sub> could be decreased (Table 1, entries 4  
111 and 9) giving almost complete selectivity to oxygenated products. Most importantly, when  
112 using low Au loading (0.25 wt.% Au/ZSM-5) the over-oxidation to CO<sub>2</sub> can be decreased to  
113 below the limit of detection (Table 1, entries 8 and 10). Lowering the temperature of reaction  
114 was also found to improve oxygenate selectivity (Supplementary Figure 8). Methane  
115 oxidation could still be observed at temperatures as low as 120 °C although the overall  
116 product yield was reduced. When using synthetic air under the equivalent reaction conditions,  
117 similar results were obtained (Supplementary Table 6) with an estimated TON of 93 based on  
118 estimated surface Au atom number (Supplementary Note 1, value based on Supplementary  
119 Table 6, entry 2). Therefore, it is clear that the catalytic oxidation of CH<sub>4</sub> with O<sub>2</sub> using  
120 Au/ZSM-5 is being achieved without the need for a co-reductant and is capable of  
121 appreciable rates (Supplementary Table 6). The catalysed reaction continues over the 2 h  
122 reaction time we have investigated (Figure 1e-h). Catalyst reuse (Supplementary Figure 9)  
123 showed that there is a small loss of activity after the first run with an increased selectivity to  
124 acetic acid.

125 These experiments have demonstrated that it is possible for methane to be selectively  
126 oxidised to C<sub>1</sub> and C<sub>2</sub> oxygenates using only molecular oxygen as the terminal oxidant in a  
127 closed catalytic cycle with significant turnover numbers. This finding can be considered to be  
128 a proof-of-concept study as methane conversions are indeed low (Supplementary Table 7)  
129 and the products that are formed are very dilute in an aqueous solution. To increase  
130 conversion, reactions at lower methane partial pressure were carried out and we achieved  
131 methane conversions of up to 4.6 % (Figure 2, Supplementary Table 7) whilst maintaining a  
132 reasonable oxygenate selectivity. At these higher conversions the products are mainly C<sub>2</sub>  
133 oxygenates.

### 134 **Catalyst characterisation**

135 A sub-set of the materials were characterised using aberration-corrected scanning  
136 transmission electron microscopy (AC-STEM), which has sufficient spatial resolution and  
137 sensitivity to identify Au species ranging from nanoparticles to sub-nm clusters to isolated  
138 atoms or cations<sup>26,27</sup>. Previous work by Shan *et al.* on atomically dispersed Rh catalysts<sup>14,15</sup>  
139 and Jin *et al.* on supported Ir-cluster catalysts<sup>28</sup> clearly demonstrated the importance of

140 isolated cations or sub -nm clusters for activating methane. Interestingly, only Au  
141 nanoparticles greater than 3 nm diameter (*i.e.*, larger than the zeolite micropores) were found  
142 in both the fresh and used 0.5 wt.% Au/ZSM-5 catalysts (Figure 3 and Supplementary Fig.  
143 10) and no sub-nm Au clusters or isolated Au atoms were detected, even for catalysts  
144 employed in multiple reuse tests (Supplementary Figure 11). ZSM-5 is known to contain Fe  
145 impurities within the porous structure<sup>11</sup> and as the Au nanoparticles are on the exterior  
146 surface of the ZSM-5 crystallites there is no possibility of any interaction between Au and Fe  
147 playing a role in the observed catalysis. Au particle size distributions were determined from  
148 bright-field TEM images (Supplementary Figure 12) and a modest increase in average  
149 particle size from 8.1 nm to 11.7-14.1 nm was found after reaction times of 2 h and 4 h. The  
150 averages seen post reaction are within the error limits of the particle size distribution (PSD).  
151 Additional AC-STEM experiments for catalysts after three 2 h reactions carried out for the  
152 reuse studies gave a PSD with a mean particle diameter of 9.8 nm (Supplementary Figure  
153 11d), indicating that there is little or no sintering of Au particles under reaction conditions or  
154 the conditions used for catalyst regeneration. Consistent particle size distributions were also  
155 observed from SEM back-scattered electron imaging, which provides a larger field of view of  
156 the sample compared to TEM/STEM analysis. Lowering the Au loading on ZSM-5  
157 (Supplementary Figure 13) from 0.5 wt.% to 0.25 wt.% and even 0.12 wt.% still resulted in  
158 Au nanoparticles having a similar mean size, but lower number densities, whereas increasing  
159 the Au loading to 1 wt.% caused significant agglomeration of the Au. We therefore infer that  
160 the active species for methane oxidation are the Au nanoparticles.

161 Fresh and used Au/ZSM-5 samples were also characterized using <sup>27</sup>Al MAS NMR, which  
162 only showed signals consistent with Al<sup>3+</sup> in the tetrahedral framework sites of the zeolite  
163 (Supplementary Figure 14). This indicates that octahedrally coordinated, extra-framework  
164 Al<sup>3+</sup> is not present in these materials and that dealumination of the zeolite does not occur  
165 under our reaction conditions.

## 166 **Computational and mechanistic studies**

167 We have explored the activation of oxygen and methane using DFT calculations (PBE+D3)  
168 with models covering periodic slabs representing stepped surfaces on large particles, Au<sub>38</sub>  
169 nanoparticles and an Au<sup>+</sup> extra-framework cation, Au<sup>+</sup>/ZSM-5 (Supplementary Figure 15).  
170 For all structures, adsorption of oxygen is accompanied by electron donation from the metal  
171 to produce an O<sub>2</sub><sup>-\*</sup> surface bound superoxo species. Figure 4 shows that, on the Au<sub>38</sub>

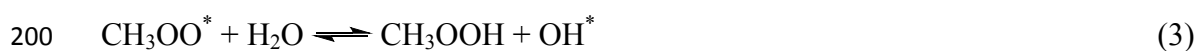
172 nanoparticle superoxo dissociation to atomic oxygen,  $2\text{O}^*$ , involves a barrier of only 39 kJ  
 173  $\text{mol}^{-1}$ , while using the stepped slab model this is somewhat higher (84 kJ  $\text{mol}^{-1}$ ). Even so, it is  
 174 clear that the larger nanoparticles observed in our electron microscopy studies should be able  
 175 to promote the dissociation of oxygen under our experimental conditions. In contrast, extra-  
 176 framework cationic gold,  $\text{Au}^{2+}\text{O}_2/\text{ZSM-5}$ , whilst strongly activating  $\text{O}_2$ , lacks an adjacent  
 177 redox centre to bind the distal oxygen. This means that  $\text{Au}^{3+}\text{O}/\text{ZSM-5}$  formation can only  
 178 proceed via hydrogen abstraction from  $\text{CH}_4$  which is blocked by a prohibitively high barrier  
 179 ( $\sim 140$  kJ  $\text{mol}^{-1}$ , Supplementary Note 2, Supplementary Figure 16). Under our experimental  
 180 conditions superoxo dissociation may also be facilitated through protonation of the molecular  
 181 adsorbate which would be favoured in acidic solution, suggesting one reason for the  
 182 improved activity seen with H-ZSM-5(25) compared to H-ZSM-5(170) (Supplementary  
 183 Figure 6 and Supplementary Table 5).

184 The activation of methane by  $\text{O}_2^*$  and  $\text{O}^*$  ([O] in equation 1) was considered for the  
 185 elementary step:



187 Generally, we find that the barrier for  $\text{O}_2^*$  to activate methane is considerably higher than  
 188 that for  $\text{O}^*$  (stepped  $\text{Au}(100)\text{O}_2$ : 124 kJ  $\text{mol}^{-1}$ ,  $\text{Au}^{2+}\text{O}_2/\text{ZSM-5}$ : 125 kJ  $\text{mol}^{-1}$ ,  $\text{Au}_{38}\text{O}_2$ : 57 kJ  
 189  $\text{mol}^{-1}$  *cf* highly stepped  $\text{Au}(100)\text{O}$ : 84 kJ  $\text{mol}^{-1}$ ,  $\text{Au}_{38}\text{O}$ : 65 kJ  $\text{mol}^{-1}$ , Supplementary Figs. 16-  
 190 19). This suggests that the dissociation of oxygen to form surface oxygen species will lead to  
 191 easier methane activation to  $\text{CH}_3^*$  on the surface of Au nanoparticles. Calculations for the  
 192 activation of  $\text{CH}_4$  over highly stepped  $\text{Au}(100)$  and  $\text{Au}_{38}$  models by O atoms are compared in  
 193 Figure 4. This highlights that the barriers involved are lower on particles of the order of 1 nm  
 194 than for larger particles of the type seen in our microscopy analysis. The 1 nm scale particles  
 195 also show a higher affinity for oxygen.

196 From the  $\text{CH}_3^*$  species produced after initial methane activation further reaction with  $\text{O}_2^*$  or  
 197  $\text{O}^*$  would be expected to lead to the  $\text{C}_1$  products, methyl hydroperoxide and methanol. For  
 198 example:





203 More intriguing is the early production of a large amount of C<sub>2</sub> products, acetic acid and  
204 peracetic acid, even in the absence of CO as a co-reductant (*e.g.* Table 1, entries 9 and 10,  
205 Figure 5c). It could be envisaged that these arise from ethane contamination of the CH<sub>4</sub> gas or  
206 coupling of CH<sub>3</sub><sup>\*</sup> during the reaction to form ethane and that ethane is oxidised to C<sub>2</sub>  
207 products. Analysis confirmed that ethane was not a contaminant of the methane used here and  
208 experiments with ethane as the reactant showed the major product to be CO<sub>2</sub> along with  
209 acetic acid and some ethanol (Supplementary Table 8). As neither ethane nor ethanol was  
210 detected during the reaction of methane (Supplementary Table 9) we concluded that ethane is  
211 not a reaction intermediate. Interestingly, methane was also observed as a product from  
212 ethane oxidation which we considered due to a reaction of ethane on the zeolite; reacting  
213 ethane with ZSM-5 in the absence of Au under the same conditions gave much higher CH<sub>4</sub>  
214 yields (Supplementary Tables 8 and 9). The zeolite also has activity for ethane oxidation, but  
215 this is enhanced by the presence of Au.

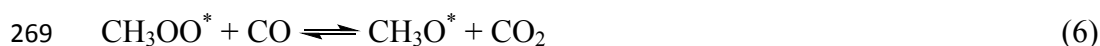
216 Given that ethane is not the source of C<sub>2</sub> products, we speculate that the intermediates  
217 CH<sub>3</sub>OO<sup>\*</sup> (reaction (2)) and CH<sub>3</sub>O<sup>\*</sup>, which lead to the C<sub>1</sub> products following reactions (4) and  
218 (5), are also involved in a further cascade of oxidation reactions to create surface bound C<sub>1</sub>  
219 species; CH<sub>2</sub>O<sup>\*</sup>, CHO<sup>\*</sup> and CO<sup>\*</sup>. These, along with CH<sub>3</sub><sup>\*</sup>, CH<sub>3</sub>O<sup>\*</sup> and CH<sub>3</sub>OO<sup>\*</sup> would  
220 establish a steady state population of C<sub>1</sub> species on the catalyst surface. Reaction of CH<sub>3</sub><sup>\*</sup>  
221 with CO<sup>\*</sup> is one possible route to a C<sub>2</sub> intermediate which will oxidise to acetic acid before  
222 being able to desorb from the catalyst surface. As Au is known to be an active catalyst for  
223 methanol carbonylation<sup>29</sup> we also performed experiments using water solvent spiked with  
224 methanol at our usual product level (Supplementary Figure 20). However, this demonstrated  
225 that methanol does not significantly re-adsorb on the catalyst to take part in the C<sub>2</sub> synthesis  
226 pathway under our reaction conditions. The idea of parallel pathways to C<sub>1</sub> and C<sub>2</sub> products  
227 led to further kinetic experiments.

228 Comparison of the temperature dependence of reactions in H<sub>2</sub>O and D<sub>2</sub>O solvents  
229 (Supplementary Table 10) shows that, although the total moles of carbon in the products  
230 produced are similar (Supplementary Figure 21a), the behaviour of the C<sub>1</sub> and C<sub>2</sub> product  
231 yields are quite different: C<sub>1</sub> products show a similar increase with temperature in both  
232 solvents, whereas C<sub>2</sub> yield increases with temperature in H<sub>2</sub>O but decreases with temperature

233 in D<sub>2</sub>O (Supplementary Figure 21b), with a correspondingly higher production of CO<sub>2</sub> in the  
234 deuterated solvent (Supplementary Figure 21a). Considering the effects on product formation  
235 of changing from H<sub>2</sub>O to D<sub>2</sub>O as a function of time (Figure 5, Supplementary Table 11), total  
236 methane conversion shows practically no kinetic isotope effect (KIE,  $k_H/k_D = 1.08$ , Figure 5a)  
237 but this conceals more substantial effects on the separate product streams, especially during  
238 the first 60 min. For example, CH<sub>3</sub>OH appearance shows  $k_H/k_D = 0.42$  during that time  
239 (Figure 5b) but the effect diminishes beyond 60 min. For the C<sub>2</sub>-oxygenates, there appears to  
240 be rapid production within the first 5 min of reaction in both solvents (Figure 5c). Thereafter,  
241 production of C<sub>2</sub> products continues in H<sub>2</sub>O and this remains a major route to oxygenated  
242 products throughout, albeit at a slower rate than during the initial period. In contrast, in D<sub>2</sub>O  
243 the formation of C<sub>2</sub> oxygenates has finished before 5 min of reaction. Correspondingly, CO<sub>2</sub>  
244 production is faster in D<sub>2</sub>O than H<sub>2</sub>O throughout,  $k_H/k_D = 0.81$  (Figure 5d). The complexity  
245 of the pattern of behaviour and the changes in KIE with time on-line suggest that several  
246 steps may involve water molecules but the KIE magnitudes indicate that none are primary  
247 KIEs arising from kinetically significant H-transfer. The largest effects are inverse KIEs,  
248 well-known in homogeneous acid-base catalysis; in the present heterogeneous system,  
249 desorption of CH<sub>3</sub>OH from surface CH<sub>3</sub>O\* might be an analogous specific hydrogen-ion  
250 catalysed process. Indeed, the low levels of product formed may mean that the adsorptive  
251 capacity of the catalyst is significant, and these desorption processes dominate the kinetic  
252 measurements. The inverse KIE on CO<sub>2</sub> formation, however, is not explicable in this way;  
253 but the very low rate of production of C<sub>2</sub> products in D<sub>2</sub>O solvent after the first 5 minutes  
254 suggests that the higher rate of CO<sub>2</sub> production in D<sub>2</sub>O is linked to differences in the C<sub>2</sub>  
255 pathway for the deuterated and normal solvents.

256 We also note that the routes to methyl hydroperoxide and methanol lead to a net oxidation of  
257 the Au nanoparticles as implied by the OH\* remaining after steps (3)-(5). In the absence of a  
258 co-reductant, methane, via reaction (1), will also serve to reduce the catalyst surface but is  
259 likely to be slow leading to blocking of sites for oxygen activation. Previous studies have  
260 shown that CO can be incorporated when added as a co-reductant for the reaction of CH<sub>4</sub> or  
261 C<sub>2</sub>H<sub>6</sub> with O<sub>2</sub><sup>14,15,28</sup> and in the proposed C<sub>1</sub> pool of surface species CO is key. Accordingly,  
262 we have also studied the addition of CO to the reactant stream (Table 1 entries 11 and 12,  
263 Supplementary Figure 22 and Supplementary Tables 4, 9 and 12). The catalyst activity was  
264 indeed found to be much higher when CO is present with TONs of up to 1400 based on  
265 estimated surface Au atom number, indicating that by addition of a co-reductant the catalytic

266 cycle can be accelerated. However, while methanol productivity is increased by an order of  
267 magnitude the increase in acetic acid is more modest. The methylhydroperoxy product is no  
268 longer observed, which we attribute to reactions of the type:



270 The activation barrier for this reaction has been estimated theoretically at 75-80 kJ mol<sup>-1</sup> in  
271 gas and liquid phase<sup>30</sup>, and so would require surface catalysis to occur at significant rate in  
272 our system. If a partial equilibrium exists between CH<sub>3</sub><sup>\*</sup> and CH<sub>3</sub>OO<sup>\*</sup>, added CO will also  
273 suppress the abundance of CH<sub>3</sub><sup>\*</sup>, which may explain the smaller increase in C<sub>2</sub> products  
274 compared to methanol. However, approximately 8 % of the added CO is oxidised to CO<sub>2</sub>, and  
275 so its dominant role is likely to be via reduction of the catalyst surface, improving the ability  
276 of the catalyst to activate O<sub>2</sub>. When CO was present, the fractional increase in the average Au  
277 particle size observed by electron microscopy after reaction was notably smaller. After a 4 h  
278 reaction with CH<sub>4</sub> (20.7 bar), O<sub>2</sub> (1.0 bar), CO (2.5 bar) the average Au particle size was 11.7  
279 nm (Supplementary Figure 12b) as opposed to 14.1 nm (Supplementary Figure 12c) for post  
280 reaction samples when no CO had been added, indicating that the presence of CO may hinder  
281 the Au agglomeration process. <sup>1</sup>H and <sup>13</sup>C NMR spectroscopy shows that the acetic acid  
282 formed from the reaction with CO present does not arise from the carbonylation of methanol  
283 and so the pathway to acetic acid is not via methanol on Au/ZSM-5 (Supplementary Figs. 23  
284 and 24) even when CO is a co-reactant. The experiments with <sup>13</sup>C enriched CH<sub>4</sub> and with <sup>13</sup>C  
285 enriched CO show that the carbon from methane appears at both positions in the acetic acid  
286 product whereas CO almost exclusively enters the carbonyl functional group (Supplementary  
287 Table 13), as would be expected from CO adding to the pool of surface bound partial  
288 oxygenates but not being hydrogenated to the more reduced species present. CO is oxidised  
289 to CO<sub>2</sub> by these catalysts but the addition of CO<sub>2</sub> itself to the reaction feed had no effect on  
290 the formation of products (Supplementary Figure 25).

## 291 **Discussion**

292 Taking into account all of the experimental data presented in our study and insights from  
293 computational work it is possible to comment further on the likely mechanism by which the  
294 observed products are formed. The resulting scheme is illustrated in Fig. 6. C<sub>1</sub> and C<sub>2</sub>  
295 oxygenates are most likely formed in separate pathways from an initial, common, surface  
296 CH<sub>3</sub><sup>\*</sup> species. Precursors for the observed methanol and methylhydroperoxide products are  
297 methoxy and methylperoxy species which we also consider to be surface bound. Given the

298 high oxygen partial pressure present in the reaction, the initial activation of methane to form  
299 surface bound  $\text{CH}_3^*$  will immediately establish an equilibrium with  $\text{CH}_3\text{OO}^*$  on the catalyst  
300 surface. We estimate that the calculated TONs (*e.g.*, Table 1, entry 9, Supplementary Note 1)  
301 corresponds to 142 molecules per particle per second across around 2200 surface Au atoms,  
302 suggesting that the surface coverage of  $\text{CH}_3\text{OO}^*$  and other metastable  $\text{C}_1$  intermediates, such  
303 as  $\text{CH}_2\text{O}^*$  and  $\text{CHO}^*$ , will be too low for reactions between such species to be significant.  
304 This implies that self-reactions between these highly reactive intermediates, commonly  
305 described in gas phase chemistry, can be excluded.

306 For the  $\text{C}_2$  oxygenates, acetic acid and peracetic acid, the analogous precursors are acyl  
307 ( $\text{CH}_3\text{CO}^*$ ) acetoxy ( $\text{CH}_3\text{C}(\text{O})\text{O}^*$ ) and acylperoxy ( $\text{CH}_3\text{C}(\text{O})\text{OO}^*$ ). Ethane oxidation in our  
308 system mainly forms  $\text{CO}_2$  (and some methane), and we find no ethane product during  
309 methane oxidation. These observations suggest that  $\text{C}_2$  formation is not via coupling of  $\text{CH}_3^*$   
310 with  $\text{CH}_3^*$ , and we propose that a surface bound acyl precursor ( $\text{CH}_3\text{CO}^*$ ) is formed via a  
311 reaction of  $\text{CH}_3^*$  with surface bound  $\text{CO}^*$  (Figure 6). We consider that an equilibrium exists  
312 between acyl and acyl peroxy that is analogous to the  $\text{CH}_3^*/\text{CH}_3\text{OO}^*$  equilibrium.

313 The early formation of  $\text{C}_2$  oxygenated products, actually before the appearance of  $\text{C}_1$   
314 oxygenates (Fig. 5c), suggests that a population of the precursors for  $\text{C}_2$  formation appears  
315 very rapidly on the catalyst surface. However, the low selectivity to  $\text{CO}_2$  throughout reaction  
316 shows that final oxidation of surface  $\text{CO}^*$  is very slow. Furthermore, desorption of  $\text{CH}_2\text{O}$  or  
317  $\text{CO}$  is not observed in our experiments. Indeed, theoretical studies have shown that  $\text{CO}$  is  
318 very strongly bound on Au surfaces<sup>Error! Reference source not found.,Error! Reference source not found.</sup> and  
319 this is consistent with  $\text{CO}$  not being observed as a product. These oxidised surface  
320 intermediates, and we propose that chemisorbed  $\text{CO}^*$  dominates, then react with the flux of  
321  $\text{CH}_3^*$  being formed by methane oxidation (or the reverse of  $\text{CH}_3\text{OO}^*$  formation (reaction 2))  
322 to form acyl, acetoxy and acylperoxy and hence yield the observed  $\text{C}_2$  oxygenate products.

323  $^{13}\text{C}$  labelling for the combined  $\text{CH}_4$  and  $\text{CO}$  oxidation experiments (Supplementary Table 13)  
324 show that the methyl group of acetic acid comes mainly from  $\text{CH}_4$  and that  $^{13}\text{C}$  labelled  $\text{CO}$   
325 in the gas phase is incorporated into the carbonyl group of the  $\text{C}_2$  oxygenated products, but  
326 with substantially lower abundance. One would expect at least some formation of  
327 chemisorbed  $\text{CO}^*$  from gas phase  $\text{CO}$ , so these labelling experiments seem consistent with  
328 our proposal of carbon-carbon bond formation between  $\text{CH}_3^*$  and  $\text{CO}^*$  to give  $\text{CH}_3\text{CO}^*$ , as  
329 the route to  $\text{C}_2$  products. The rather slow oxidation of  $\text{CO}$  in  $\text{CO}$  only experiments  
330 (Supplementary Table 12), and the absence of any observed  $\text{CO}$  product in methane  
331 oxidation, also suggest a substantial barrier to exchange between gas phase  $\text{CO}$  and  $\text{CO}^*$ .

332 The very rapid initial formation of C<sub>2</sub> oxygenates in H<sub>2</sub>O as the solvent is followed by  
 333 sustained production which remains a major reaction path (Fig. 5c). In contrast, methanol  
 334 appears at a steadier rate throughout the reaction (Fig. 5b). In D<sub>2</sub>O as the solvent, similar  
 335 initial formation of C<sub>2</sub> oxygenates is observed (Fig. 5c), but then stops. These observations  
 336 suggest an initial state of the fresh catalyst (for example the presence of H<sup>+</sup>, OH\* or H<sub>2</sub>O\*)  
 337 that enables rapid reaction of methane to form the distribution of surface C<sub>1</sub> intermediates we  
 338 have described above, as well as the formation and release of C<sub>2</sub> oxygenates. In H<sub>2</sub>O solvent,  
 339 key surface species are replenished and the formation and release of C<sub>2</sub> products continues,  
 340 but at a somewhat slower rate. Since formation of C<sub>1</sub> and C<sub>2</sub> oxygenates compete for CH<sub>3</sub>\*,  
 341 this slowing of the C<sub>2</sub> formation rate may be why C<sub>1</sub> oxygenate formation then appears at a  
 342 steady rate. In D<sub>2</sub>O as solvent, the same initial state of the fresh catalyst again causes early  
 343 formation of C<sub>2</sub> oxygenates, but the key surface species are no longer replenished and C<sub>2</sub>  
 344 formation then stops. It should be noted that CO<sub>2</sub> formation continues in D<sub>2</sub>O, at a somewhat  
 345 higher rate than in H<sub>2</sub>O (Fig. 5d), so the cascade of C<sub>1</sub> oxygenated species from CH<sub>3</sub>\* to CO\*  
 346 continues in both solvents. These combined observations suggest a key role for hydrogen  
 347 containing surface species in enabling the formation and release of C<sub>2</sub> oxygenates, for  
 348 example H<sup>+</sup>, OH\* or H<sub>2</sub>O\*. We consider that one possibility is that the carbon-carbon bond  
 349 forming, reaction (7), is reversible.



350 Then the fate of CO\* is governed by competition between reactions (8) and (9):  
 351



352  
 353  
 354 The hydrolysis step required to convert CH<sub>3</sub>CO\* to acetic acid will be slower in D<sub>2</sub>O than  
 355 H<sub>2</sub>O so that the competition for reversing the C-C bond formation and then losing CO\* by  
 356 oxidation to CO<sub>2</sub> will reduce the rate of C<sub>2</sub> formation.  
 357

358 The main effect of adding CO to the methane oxidation system is to substantially increase the  
 359 rate of methane oxidation and methanol formation (Table 1). We propose that this is due to  
 360 CO maintaining the catalyst in a reduced state. There is an interesting secondary effect of  
 361 added CO on the product distribution. Whereas the methanol yield increases by more than an  
 362 order of magnitude, the methyl hydroperoxide yield becomes negligible. This may be due to  
 363 the surface analogue of a known reaction<sup>30</sup> between CH<sub>3</sub>OO and CO (equation (6)) which  
 364 would switch products away from methyl hydroperoxide to methanol. In contrast to C<sub>1</sub>  
 365 oxygenates, addition of CO increases C<sub>2</sub> oxygenate yield only modestly. This may be due to

366 the rate of formation of C<sub>2</sub> products being lower on the reduced catalyst that will be present  
367 in the presence of CO; or could also be caused by a rapid reaction of CO with CH<sub>3</sub>OO\*  
368 which will also impact the standing CH<sub>3</sub>\* concentration via the reversible equilibrium  
369 between these two species. Hence, despite a large increase in the flux of CH<sub>3</sub>\* formation, its  
370 standing concentration increases only modestly, and the reaction of CH<sub>3</sub>\* with CO\* does not  
371 greatly change.

372 In conclusion, we have shown that Au nanoparticles supported on ZSM-5 can oxidise CH<sub>4</sub> to  
373 methanol and acetic acid with minimal formation of CO<sub>2</sub>. Although comparison between  
374 batch and flow reactor conditions can only be qualitative it is possible to make some  
375 important considerations. We report, in our batch experiments, a maximum oxygenate  
376 productivity at short times of 7.3 mol/mol<sub>Au</sub>/h (37 mmol/g<sub>Au</sub>/h) (Table 1, entry 10). Even at 1  
377 h of reaction time a productivity of 1.9 mol/mol<sub>Au</sub>/h (9.5 mmol/g<sub>Au</sub>/h) is observed which is  
378 higher than that reported for Cu-based catalysts tested under similar conditions under flow  
379 conditions (Supplementary Table 2)<sup>22,23</sup>. In contrast to the Cu-zeolite catalysts previously  
380 reported for which only C<sub>1</sub> products are observed, C<sub>2</sub> oxygenates are the major products  
381 observed with the Au-ZSM-5 catalyst demonstrating that the Au catalyst operates by a  
382 different mechanism. Importantly, we observe this reaction in the absence of a co-reductant,  
383 and we show that the mechanism largely involves surface bound intermediates rather than  
384 species in the fluid phase.

385

## 386 **Methods**

387

### 388 **Note on safe operation of experiments**

389 Any reaction involving catalytic oxidation must take care to work under conditions outside of  
390 the explosive mixture composition of the reagents. In the case of methane with oxygen C M  
391 Cooper and P J Wiezevich have shown that as long as the experiments are conducted at ≤  
392 14% O<sub>2</sub> even at elevated temperature and pressure the experiment is outside of the explosive  
393 regime.<sup>33</sup> This is the case for all our experiments.

394 **Catalyst Preparation.** H-ZSM-5 zeolites with SiO<sub>2</sub>/Al<sub>2</sub>O<sub>3</sub> of 23, 25, 50 and 170 were  
395 obtained from Nankai University catalyst company Co., Ltd and Zeolyst International. H-  
396 ZSM-5 with SiO<sub>2</sub>/Al<sub>2</sub>O<sub>3</sub> of 25 was used as support for Au loading unless specified otherwise.  
397 Gold(III) chloride trihydrate (HAuCl<sub>4</sub>·3H<sub>2</sub>O, ≥49.0% Au basis) was purchased from Merck.  
398 SiO<sub>2</sub> (particle size: 30 nm) and γ-Al<sub>2</sub>O<sub>3</sub> (particle size: 30 nm) were obtained from the Aladdin

399 Chemical Reagent Co., Ltd. Aqueous ammonia (25-28 %), sodium carbonate (99.8%),  
400 sodium hydroxide ( $\geq 96\%$ ) and hydrochloric acid (37%) were obtained from Sinopharm  
401 Chemical Reagent Co., Ltd. Methane (99.999%), ethane (99.9%) and carbon monoxide  
402 (99.999%) were obtained from Dalian Special Gases Co., Ltd. D<sub>2</sub>O (<sup>2</sup>H, 99.9%) was  
403 purchased from Qingdao Tenglong Weibo Technology Co., Ltd. Nitrogen (99.999%), oxygen  
404 (99.999%) and synthetic air (21% O<sub>2</sub> and 79% N<sub>2</sub>) were obtained from Wuhan Huaxing  
405 Industrial Gas Co., Ltd. <sup>13</sup>CH<sub>4</sub> (<sup>13</sup>C, 99%) and <sup>13</sup>CO (<sup>13</sup>C, 99%) was purchased from  
406 Cambridge Isotope Laboratories, Inc. All materials and reagents were used directly without  
407 purification.

408 Au loaded catalysts were prepared by a deposition-precipitation methodology using aqueous  
409 ammonia as the base to control the pH value. Typically, 3.0 g of zeolite/support dispersed in  
410 200 ml of deionized water and a known amount of 6.0 mmol/L HAuCl<sub>4</sub> aqueous solution  
411 were mixed in a flat bottom beaker under stirring at 600 rpm. An appropriate amount of 2.5  
412 wt.% aqueous ammonia solution was slowly dropped into the above solution until the  
413 expected pH value was achieved. This step took more than 30 min at room temperature. The  
414 resulting solution was aged in a pre-heated water bath at 60 °C for 2 h under stirring at 600  
415 rpm. Then, the sample was filtered and fully washed with deionized water. After drying in an  
416 oven at 60 °C overnight, the sample was further calcined in a tubular furnace in static air. The  
417 temperature was programmed from room temperature to 240 °C at 3 °C/min and kept at 240  
418 °C for 90 min, and then cooled to room temperature.

419 **Catalyst Characterization.** XRD patterns were recorded on a Panalytical X'Pert PRO X-ray  
420 diffractometer (40 kV, 40 mA) using Cu K $\alpha$  ( $\lambda=1.5406$  Å) radiation with scan rate 0.2° s<sup>-1</sup>.  
421 The Au4f XPS spectra were collected using a Thermo Fisher Scientific K-Alpha spectrometer  
422 using an Al K $\alpha$  source with pass energy 150.0 eV. The photoelectron peak of C1s, located at  
423 284.8 eV, was used as reference for binding energies in all XPS spectra. BET surface area  
424 was obtained by nitrogen isotherms at -196 °C using a Micromeritics ASAP 2020 M system.  
425 Samples were outgassed for 10 h at 200 °C before the measurements. Au and Fe content in  
426 the catalysts was determined by inductively coupled plasma Optical Emission Spectrometry  
427 (ICP-OES) with an Agilent 700 spectrometer. The Au/ZSM-5 catalysts were structurally  
428 characterized using a combination of scanning electron microscopy (SEM), transmission  
429 electron microscopy (TEM) and scanning transmission electron microscopy (STEM). SEM  
430 back-scattered electron (BSE) imaging was carried out at Cardiff University on a TESCAN  
431 MAIA3 microscope equipped with a Schottky gun operating at 30 kV. Samples for TEM and  
432 STEM analysis were dry mounted onto holey carbon film TEM grids. TEM bright field (BF)

433 imaging experiments were carried out at Cardiff University using a JEOL 2100 microscope  
434 equipped with a LaB<sub>6</sub> electron gun operating at 200 kV. Particle size distributions were  
435 determined from these BF-TEM images using ImageJ in which a minimum of 300 particles  
436 were counted for each specimen. STEM high angle annular dark field (HAADF) imaging was  
437 performed at the National University of Singapore, using an aberration-corrected JEOL  
438 ARM200CF microscope equipped with a cold field-emission gun operating at 200 kV. <sup>27</sup>Al  
439 MAS NMR experiments were carried out at 9.4 T on a Bruker Avance III 400 spectrometer  
440 with a 4 mm double-resonance probe. The resonance frequency was 104.05 MHz for <sup>27</sup>Al.  
441 The spectra were acquired by small-flip angle technique with a pulse length of 0.2 μs  
442 (corresponding to a π/18 flip angle) and a recycle of delay of 1s. The <sup>27</sup>Al chemical shifts  
443 were referenced to 1M Al(NO<sub>3</sub>)<sub>3</sub> aqueous solution (0 ppm). The magic angle spinning rate  
444 was set to 10 kHz.

445 **Catalyst Testing.** Methane oxidation with oxygen was carried out in a 25 mL stainless steel  
446 Parr autoclave reactor. In general, 0.1 g catalyst and 15 mL deionized water were transferred  
447 into the reactor and the reactor was sealed and bubbled with pure nitrogen for more than 30  
448 min to remove dissolved gas. After purging three times with methane, the reactor was  
449 pressurized with a gas mixture of methane and oxygen. The total pressure was set at 24.2 bar  
450 with varied methane and oxygen (0.14~3.5 bar) partial pressures measured at room  
451 temperature. The mixture was initially stirred at 1000 rpm for 10 min at room temperature  
452 and the pressure stayed constant at around 24 bar. The reactor was then heated to the desired  
453 reaction temperature (120-240 °C) within 30 min and maintained at the reaction temperature  
454 for 5 min to 2 h. The reaction was stopped by cooling in ice water to a temperature below 10  
455 °C in order to minimize the loss of volatile products. Gas in the head space of the reactor was  
456 collected for analysis in a gas sampling bag at the end of a reaction. Liquid products were  
457 sampled using a glass syringe with Teflon filter head for NMR analysis. Heavy water was  
458 used in place of water as the solvent and the reactions were performed at the same condition  
459 to that using water as solvent.

460 Methane oxidation using synthetic air as oxidant was performed with the same procedure. Air  
461 partial pressure in the reaction varied from 0.67 to 4.2 bar and the total pressure was balanced  
462 to be 24.2 bar with methane. The reaction was performed at 240 °C for times as reported.

463 For reactions of methane, oxygen and CO (or CO<sub>2</sub>), various oxygen and CO (CO<sub>2</sub>) partial  
464 pressures (0 to 2.5 bar) were used and the total pressure was balanced to be 24.2 with  
465 methane. Generally, the reaction was performed at 240 °C for 1-4 h.

466 Ethane was compared with methane for the oxidation reactions under the same conditions.

467 To test the role of methanol in the reaction mechanism methanol solution with the conditions  
468 specified in Supplementary Fig. 23.

469 Reactions in D<sub>2</sub>O solvents were carried out at a series of temperatures from 120 °C to 240 °C  
470 using the standard experimental procedure and gas composition described above  
471 (Supplementary Table 10) for catalysts with 0.5 wt.% Au loading.

472

473 **Isotopic tracer experiments.** To trace the fate of carbon atoms from methane, CH<sub>4</sub> with 6%  
474 <sup>13</sup>C-labeled mixed with 94% in natural abundance was used in the co-reaction with oxygen  
475 and CO. The reactions were performed at 240 °C for 1 or 4 h with initial partial pressure of  
476 20.7 bar, 1.0 bar and 2.5 bar for CH<sub>4</sub>, O<sub>2</sub> and CO respectively (Gases charged to the autoclave  
477 at room temperature). CO (6% <sup>13</sup>C-labeled mixed with 94% in natural abundance) was  
478 alternatively used to trace the fate of carbon atom from CO in the co-reactions under the same  
479 conditions.

480 A high-sensitivity NMR CryoProbe on a Bruker Avance-600 liquid NMR spectrometer was  
481 employed to analyze the liquid products obtained from the isotopic tracing experiments. <sup>1</sup>H  
482 NMR spectra were recorded using a water suppression pulse sequence. <sup>1</sup>H-<sup>13</sup>C heteronuclear  
483 multiple-bond correlation (HMBC) experiments were performed for the analysis of <sup>13</sup>C  
484 labelling in methanol and acetic acid.

485 In the <sup>1</sup>H NMR spectra (Supplementary Fig. 24a), the protons attached to methyl groups of  
486 methanol and acetic acid produce doublet due to the spin-spin splitting by enriched <sup>13</sup>C atom.  
487 The integral of the doublet shows the abundance of the <sup>13</sup>C atom in the methyl group.  
488 Together with the <sup>1</sup>H-<sup>13</sup>C HMBC spectra (Supplementary Fig. 24b), the abundance of <sup>13</sup>C  
489 atom on carbonyl group of acetic acid can be obtained. The details are shown in  
490 Supplementary Table 13.

491 **Time on-line measurements.** The reaction yields were measured for a series of reaction  
492 times to build up a picture of the evolution of products as the reaction proceeds in both H<sub>2</sub>O  
493 and D<sub>2</sub>O solvents (Fig. 5, Supplementary Fig. 21, Supplementary Table 11). For these  
494 experiments, the reaction temperature was lowered to 200 °C in order to ensure good  
495 resolution of the kinetic curves at short reaction times. The gas mixture was also altered to  
496 CH<sub>4</sub> (20.7 bar), O<sub>2</sub> (1 bar) with N<sub>2</sub> at (2.5 bar) added to maintain a total gas pressure  
497 consistent with earlier experiments. The reactor design used here with significant gas  
498 pressure in the autoclave headspace means that the time online data of Fig. 5, Supplementary  
499 Fig. 21, Supplementary Table 11 did come not from a sampling procedure but from  
500 collections of single experiments for each point. To achieve this fresh catalyst samples were

501 used in the reactor for each time point recorded and so we expect that trends are thus more  
502 reliable than individual data points.

503 **Product analysis.** The gaseous products analysis was performed on a Shimadzu GC-2014C  
504 Gas chromatography system equipped with a methanizer-unit and FID detector using a TDX-  
505 01 packed column. The liquid products were quantified by  $^1\text{H}$  NMR on a Bruker Avance-600  
506 liquid NMR spectrometer using a water suppression pulse sequence (Watergate5).<sup>34</sup> The  
507 measurement was calibrated using an external standard method with a series of methanol  
508 solutions with known concentrations. The experimental error bounds were determined as  
509  $\pm 5\%$ . Typically, 0.4 mL of liquor after reaction was mixed with 0.1 mL of heavy water to  
510 prepare a solution for NMR measurement. The concentration (mmol/L) of each liquid  
511 product was determined based on the calibration plot (Supplementary Fig. 4).

512 The dissolved  $\text{CO}_2$  in reaction solution was analysed with the headspace sampling method on  
513 GC proposed by Sarradin and Caprais.<sup>35</sup> A 25 mL gas-tight syringe with seal valve was used  
514 in place of headspace flask. Typically, 10 ml of the fresh reaction solution (the catalyst still  
515 present) and 0.1 mL of hydrochloric acid (6 mol/L) was quickly taken into the syringe under  
516 a nitrogen atmosphere. Then the syringe was filled with nitrogen to a volume of 20 mL. After  
517 that, the syringe was heated for 30 min at 70 °C and shaken for 30 seconds. This operation  
518 was repeated several times in order to completely extract  $\text{CO}_2$ . The gas in the syringe was  
519 analysed on a Shimadzu GC-2014C Gas Chromatography system equipped with a  
520 methanizer-unit and FID detector using a TDX-01 packed column. The productivity of  $\text{CO}_2$   
521 was calibrated by standard gas. The results for a standard reaction are shown in  
522 Supplementary Table 14 and show that only minimal  $\text{CO}_2$  was dissolved in the water used in  
523 the reaction. To estimate the error in measured productivity four repeat experiments were  
524 performed giving a standard deviation of between 9 and 12 % (Supplementary Table 15).

525 **Electronic Structure Calculations.** All calculations were performed using the Vienna Ab  
526 initio Simulation Package (VASP)<sup>36,37</sup> with the generalized gradient approximation (GGA)  
527 functional of Perdew, Burke and Ernzerhof (PBE).<sup>38</sup> Grimme D3 level dispersion<sup>39</sup> was also  
528 included to account for attractive van der Waals forces between adsorbates and surfaces. All  
529 calculations were carried out spin unrestricted unless otherwise stated. The Projector  
530 Augmented Wave method (PAW) was used for core states.<sup>40,41</sup> For gold this means that there  
531 are 60 core electrons represented by PAW and the states for 19 valence electrons are  
532 calculated explicitly. All geometry relaxations on the nanoparticle system were performed  
533 with electronic and geometric convergence criteria set to  $10^{-6}$  eV and  $0.01 \text{ eV \AA}^{-1}$  or lower,  
534 respectively, calculations on the extra framework cationic system used a  $10^{-5}$  eV electronic

535 cut-off.

536 For reaction barriers, initial estimates of the transition state were made from the minimum  
537 energy path between reactants and products using either the Nudged Elastic Band (NEB)<sup>42</sup>  
538 method or with atom distance constraints for bonds breaking/forming in a given elementary  
539 steps implemented within the Atomic Simulation Environment (ASE).<sup>43</sup> NEB barriers were  
540 usually refined with the climbing image modification developed by Henkelmen and co-  
541 workers.<sup>44,45</sup> We use between 5 and 10 images in NEB calculations with the initial  
542 interpolation carried out using linear interpolation for diatomic dissociation and a group  
543 centred interpolation approach<sup>46</sup> for more complex cases. In the constrained optimisation  
544 method with ASE a particular atom-atom distance (C..H or O..H) was incremented using an  
545 initial step size of 0.2 Å to identify the region of the saddle point and at each step the system  
546 was optimized to a level of 0.05 eV Å<sup>-1</sup> under the imposed constraint before the next  
547 atom..atom distance increment took place. This region was then further refined using a step  
548 size of 0.03 Å. NEB or bond scan transition state estimates were used for transition state  
549 optimisation using the dimer method<sup>44</sup> with a geometry convergence of 0.05 eV Å<sup>-1</sup>.  
550 Transition states were verified by performing a frequency calculation on the proposed  
551 transition state and confirming a single imaginary mode.

552 Three classes of model were constructed to represent the Au species that could be present in  
553 the active catalyst are shown in Supplementary Fig. 15. Electron microscopy images show  
554 rounded particle morphologies (Supplementary Fig. 10) and particle size distributions  
555 (Supplementary Fig. 12) show that Au is present exclusively as relatively large nanoparticles  
556 with average particle sizes of 8.1 nm for fresh materials and 14.1 nm for used catalysts. To  
557 model the surfaces of these particles periodic slab calculations were used for the flat Au(111)  
558 and Au(100) planes. To represent the irregular surface features of the rounded particles a  
559 stepped surface model was also constructed by removing rows of atoms from the Au(100)  
560 slab to give steps with (111) edges (Supplementary Fig. 15a). The Au(111) and Au(100) slab  
561 models were generated by cleaving the optimised bulk fcc unit cell. In both cases, 5 atomic  
562 layers were used and supercells in the surface vectors consisting of a (2×2) expansion for the  
563 (111) slab and a (3×3) expansion for the (100) case so that the number of atoms in the (111)  
564 and (100) slabs was set to 80 and 90 atoms respectively. A vacuum gap of 13 Å was  
565 employed and the bottom three layers of each slab were fixed at their optimised bulk co-  
566 ordinates. The plane wave cut off for slab calculations was set to 400 eV based on  
567 convergence of the bulk unit cell energy. A dipole correction along the z-direction of the slab,  
568 perpendicular to the exposed surface, was included in all calculations. For the original

569 optimisation of the bulk structure  $k$ -point sampling of  $7 \times 7 \times 7$  was used. The larger unit cells  
570 of the slab calculations allowed this to be reduced to  $3 \times 3 \times 1$ . For the Au cation system, no  
571 vacuum gap was required as all important surfaces were internal.

572 It is also possible that, under reaction conditions, the particles seen in electron microscopy  
573 could act as reservoirs for smaller nanoparticles or even for ion exchange of Au cations into  
574 the zeolite pore structure. Accordingly, we also considered the ability of sub-nanometer metal  
575 particles (Supplementary Fig. 15b) and extra-framework Au cations (Supplementary Fig. 15c)  
576 to act as catalytic sites for the activation of oxygen and methane.

577 The sub-nanometer Au particles contained 38 atoms in a truncated octahedral geometry  
578 (Supplementary Fig. 15b) were placed within a cubic periodic box with edges of 25 Å. A  
579 plane wave cut-off of 500 eV was found to be sufficient to converge the total energy of Au<sub>38</sub>  
580 nanoparticles to less than 0.008 eV. For these isolated nanoparticles only the  $\Gamma$ -point is  
581 needed in reciprocal space ( $k$ -point grid sampling  $1 \times 1 \times 1$ ). For the Au<sub>38</sub> particles Gaussian  
582 smearing with a very small width of 0.001 was employed to represent the discrete nature of  
583 the states within the particle. For all geometry relaxation calculations, all atoms of adsorbate  
584 and clusters were free to move with no atomic restraints applied.

585 To represent Au acting as an extra-framework cation in the ZSM-5 framework, the model  
586 shown in Supplementary Fig. 15c was constructed. Here, a single tetrahedral site in a purely  
587 SiO<sub>4</sub> MFI framework (the structure of ZSM-5) is substituted with aluminum at the T12 site to  
588 give the extra-framework Au cation a formal oxidation state of +1 situated near to the  
589 junction of the straight and sinusoidal channel. A  $k$ -point mesh of  $3 \times 3 \times 3$  was used for  
590 optimization and transition state calculations for the resulting Au<sup>+</sup>/ZSM-5 model.

591 The energy,  $E$ , as used in the various potential energy diagram figures, for molecular species  
592 was calculated as:

$$593 \quad E = E_{cl+m} - E_{cl} - E_m \quad (10)$$

594 Where,  $E_{cl+m}$ , is the calculated total energy for the optimised active site model (slab, cluster  
595 or Au<sup>+</sup>/ZSM-5) model with the adsorbate in a given location,  $E_{cl}$ , is the calculated total  
596 energy for the optimised cluster or slab alone and  $E_m$ , is the calculated total energy for the  
597 optimised molecule alone, effectively in the gas phase. All three calculations employ the  
598 same periodic simulation cell and calculation parameters as defined above. For multiple  
599 adsorbates, *e.g.* O<sub>2</sub> and CH<sub>4</sub>, potential energy diagrams were produced based on the stable gas  
600 phase species and the relevant clean cluster, surface or empty Au<sup>+</sup>/ZSM-5 zeolite. The  
601 oxygen reference was always taken as the triplet ground state of the O<sub>2</sub> molecule.

602

603 **Data Availability**

604 All data used in this publication is available free of charge from Cardiff University via  
605 <http://doi.org/10.17035/d.2021.0142278187> or available from the authors upon reasonable  
606 request.

607

608 **Author Contributions**

609 J.X. and G.J.H conceived the research idea and organized the research programs. G.Q. and  
610 R.J.L. prepared catalyst samples, G. Q., X.Z. and F.D. performed the catalytic experiments  
611 and NMR analysis, T.E.D, Q.H., A.G.R.H. obtained electron microscopy data under the  
612 direction of C.J.K.. D.J.W., A.N, M.A.S. and M.Q. carried out most of the computational  
613 chemistry calculations. D.B. and M.J.H. provided mechanistic interpretation of results along  
614 with C.R.A.C and D.J.W. who integrated experimental and computational insights. B.A.M.  
615 and B.H. provided advice on the industrial context of the work. J.X., G.J.H. and D.J.W. wrote  
616 the paper and all authors discussed the results and the various revisions of the manuscript.  
617 J.X. and G.J.H. contributed equally to this work.

618 **Competing Interests**

619 The authors declare no competing interests.

620 **Acknowledgements**

621 This work was financially supported by the National Natural Science Foundation of China  
622 (Grants U1932218, 21872170, 21733013, 22061130202), Key projects of international  
623 partnership plan for foreign cooperation (112942KYSB20180009). JX thanks the Royal  
624 Society and the Newton Fund for Royal Society—Newton Advanced Fellowship. GJH.  
625 acknowledges the support from the Chinese Academy of Sciences (CAS) President's  
626 International Fellowship Initiative (PIFI) (Grant No. 2019DM0015). QH thanks the support  
627 from National Research Foundation (NRF) Singapore, under its NRF Fellowship (NRF-  
628 NRFF11-2019-0002). We thank Cardiff University and the Max Planck Centre for  
629 Fundamental Heterogeneous Catalysis (FUNCAT) for financial support. GJH, DJW and  
630 CRAC would like to thank the EPSRC for funding this work (Grant reference codes:  
631 EP/P033695/1 and EP/L027240/1). Via our membership of the UK's HEC Materials  
632 Chemistry Consortium, which is funded by EPSRC (EP/L000202, EP/R029431), this work  
633 used the ARCHER UK National Supercomputing Service (<http://www.archer.ac.uk>) and the

634 UK Materials and Molecular Modelling Hub for computational resources, MMM Hub, which  
635 is partially funded by EPSRC (EP/P020194).

636

637

638 **References**

- 639 1. Hammer, G. et al. *Natural Gas in Ullmann's Encyclopaedia of Industrial Chemistry*.  
640 (Wiley-VCH, Weinheim, 2012).
- 641 2. Gesser, H. D., Hunter, N. R. & Prakash, C. B. The direct conversion of methane to  
642 methanol by controlled oxidation. *Chem Rev.* **85**, 235-244 (1985).
- 643 3. Conley, B. L. et al. Design and study of homogenous catalysts for the selective, low  
644 temperature oxidation of hydrocarbons. *J. Mol. Cat. A: Chem.* **251**, 8-23 (2006).
- 645 4. Hargreaves, J. S. J., Hutchings, G. J. & Joyner, R. W. Control of product selectivity in  
646 the partial oxidation of methane. *Nature*, **348** 428-429 (1990).
- 647 5. Periana, R. A. et al. A mercury-catalyzed, high-yield system for the oxidation of  
648 methane to methanol. *Science* **259**, 340-343 (1993).
- 649 6. Periana, R. A. et al. Platinum catalysts for the high-yield oxidation of methane to a  
650 methanol derivative. *Science* **280**, 560-564 (1998).
- 651 7. Sobolev, V. I., Dubkov, K. A., Panna, O. V. & Panov, G. I. Selective oxidation of  
652 methane to methanol on a FeZSM-5 surface. *Catal. Today* **24**, 251-252 (1995).
- 653 8. Starokon, E. V. et al. Oxidation of methane to methanol on the surface of FeZSM-5  
654 zeolite. *J. Catal.* **300**, 47-54 (2013).
- 655 9. Starokon, E. V., Parfenov, M. V., Pirutko, L. V., Abornev, S. I. & Panov, G. I.  
656 Room-temperature oxidation of methane by  $\alpha$ -oxygen and extraction of products from  
657 the FeZSM-5 surface. *J. Phys. Chem. C* **115**, 2155-2161 (2011).
- 658 10. Parfenov, M. V., Starokon, E. V., Pirutko, L. V. & Panov, G. I. Quasicatalytic and  
659 catalytic oxidation of methane to methanol by nitrous oxide over FeZSM-5 zeolite. *J.*  
660 *Catal.* **318**, 14-21 (2014).
- 661 11. Hammond, C. et al. Direct catalytic conversion of methane to methanol in an aqueous  
662 medium by using copper-promoted Fe-ZSM-5. *Angew. Chem. Intl. Ed.* **51**, 5129-5133  
663 (2012).
- 664 12. Yu, T. et al. Highly Selective Oxidation of Methane into Methanol over Cu-Promoted  
665 Monomeric Fe/ZSM-5. *ACS Catal.* **11**, 6684-6691 (2021).
- 666 13. Narsimhan, K et al. Methane to acetic acid over Cu-exchanged zeolites: mechanistic  
667 insights from a site-specific carbonylation reaction. *J. Am. Chem. Soc.* **137**, 1825-  
668 1832 (2015).
- 669 14. Shan, J., Li, M., Allard, L. F., Lee, S. & Flytzani-Stephanopoulos, M. Mild oxidation  
670 of methane to methanol or acetic acid on supported isolated rhodium catalysts,

- 671 *Nature*, **551**, 605-608 (2017).
- 672 15. Tang, Y. et al. Single rhodium atoms anchored in micropores for efficient  
673 transformation of methane under mild conditions, *Nature Commun.* **9**, 1231 (2018).
- 674 16. Jin, Z. et al. Hydrophobic zeolite modification for in situ peroxide formation in  
675 methane oxidation to methanol, *Science* **367**, 193-197 (2020).
- 676 17. Agarwal, N. et al. Aqueous Au-Pd colloids catalyze selective CH<sub>4</sub> oxidation to  
677 CH<sub>3</sub>OH with O<sub>2</sub> under mild conditions. *Science* **358**, 223-226 (2017).
- 678 18. Groothaert, M. H., Smeets, P. J., Sels, B. F., Jacobs, P. A. & Schoonheydt, R. A.  
679 Selective oxidation of methane by the bis( $\mu$ -oxo)dicopper core stabilized on ZSM-5  
680 and mordenite zeolites. *J. Am. Chem. Soc.* **127**, 1394-1395 (2005).
- 681 19. Patrick, T. et al. Isothermal cyclic conversion of methane into methanol over copper-  
682 exchanged zeolite at low temperature. *Angew. Chem. Intl. Ed.* **55**, 5467-5471 (2016).
- 683 20. Grundner, S. et al. Single-site trinuclear copper oxygen clusters in mordenite for  
684 selective conversion of methane to methanol. *Nature Comm.* **6**, 7546 (2015).
- 685 21. Sushkevich, V. L., Palagin, D., Ranocchiari, M. & van Bokhoven, J. A. Selective  
686 anaerobic oxidation of methane enables direct synthesis of methanol. *Science* **356**,  
687 523-527 (2017).
- 688 22. Narsimhan, K., Iyoki, K., Dinh, K. & Román-Leshkov, Y. Catalytic oxidation of  
689 methane into methanol over copper-exchanged zeolites with oxygen at low  
690 temperature. *ACS Central Sci.* **2**, 424-429 (2016).
- 691 23. Dinh, K.T., Sullivan, M.M., Narsimhan, K., Serna, P., Meyer, R.J., Dinca, M. Roman-  
692 Leshkov, Y. Continuous partial oxidation of methane to methanol catalyzed by  
693 diffusion-paired copper dimers in copper-exchanged zeolites. *J. Amer. Chem. Soc.*  
694 **141**, 11641–11650 (2019).
- 695 24. Koishybay, A. & Shantz, D.F., Water is the oxygen source for methanol produced in  
696 partial oxidation of methane in a flow reactor over Cu-SSZ-13. *J. Amer. Chem. Soc.*  
697 **142**, 11962–11966 (2020).
- 698 25. Sarv, P. et al., Mobility of the acidic proton in Brønsted sites of H-Y, H-Mordenite,  
699 and H-ZSM-5 Zeolites, studied by high-temperature <sup>1</sup>H MAS NMR. *J. Phys. Chem.*,  
700 **99**, 13763-13768 (1995).
- 701 26. Herzog, A. A, Kiely, C. J., Carley, A. F., Landon, P. & Hutchings, G. J. Identification  
702 of active gold nanoclusters on iron oxide supports for CO oxidation. *Science.* **321**,  
703 1331–1335 (2008).

- 704 27. He, Q. et al. Population and hierarchy of active species in gold iron oxide catalysts for  
705 carbon monoxide oxidation. *Nat. Commun.* **7**, 12905 (2016).
- 706 28. Jin, R. et al. Low temperature oxidation of ethane to oxygenates by oxygen over  
707 iridium-cluster catalysts. *J. Am. Chem. Soc.* **141**, 18921-18925 (2019).
- 708 29. Gouget, A. et al. Increased dispersion of supported gold during methanol  
709 carbonylation. *J. Am. Chem. Soc.* **131**, 6973-6975 (2009).
- 710 30. Denisov, E. T. & Shestakov, A. F. Reactions of Alkoxy and Peroxy Radicals with  
711 Carbon Monoxide. *Kinet. Catal.*, **49**, 1–10 (2008).
- 712 31. Boronat, M., Concepción, P. & Corma, A. Unravelling the Nature of Gold Surface  
713 Sites by Combining IR Spectroscopy and DFT Calculations. Implications in Catalysis.  
714 *J. Phys. Chem. C* **113**, 16772-16784 (2009).
- 715 32. Liu, Z-P., Hu, P. & Alavi, A., Catalytic Role of Gold in Gold-Based Catalysts: A  
716 Density Functional Theory Study on the CO Oxidation on Gold. *J. Amer. Chem. Soc.*  
717 **124**, 14770–14779 (2002).
- 718 33. Cooper, C. M. & Wiezevich, P. J. Effects of Temperature and Pressure on the Upper  
719 Explosive Limit of Methane-Oxygen Mixtures. *Ind. Eng. Chem.* **21**, 1210–1214  
720 (1929).
- 721 34. Liu, M. *et al.* Improved WATERGATE Pulse Sequences for Solvent Suppression in  
722 NMR Spectroscopy. *J. Magn. Reson.* **132**, 125–129 (1998).
- 723 35. Sarradin, P.-M. & Caprais, J.-C. Analysis of dissolved gases by headspace sampling  
724 gas chromatography with column and detector switching. Preliminary results. *Anal.*  
725 *Commun.* **33**, 371-373 (1996).
- 726 36. Kresse, G. & Hafner, J. *Ab initio* molecular dynamics for liquid metals. *Phys. Rev. B*  
727 **47**, 558–561 (1993).
- 728 37. Kresse, G. & Furthmüller, J. Efficient iterative schemes for *ab initio* total-energy  
729 calculations using a plane-wave basis set. *Phys. Rev. B* **54**, 11169–11186 (1996).
- 730 38. Perdew, J. P., Burke, K. & Ernzerhof, M. Generalized Gradient Approximation Made  
731 Simple. *Phys. Rev. Lett.* **77**, 3865–3868 (1996).
- 732 39. Grimme, S., Antony, J., Ehrlich, S. & Krieg, H. A consistent and accurate *ab initio*  
733 parametrization of density functional dispersion correction (DFT-D) for the 94  
734 elements H-Pu. *J. Chem. Phys.* **132**, 154104 (2010).
- 735 40. Kresse, G. & Joubert, D. From ultrasoft pseudopotentials to the projector augmented-  
736 wave method. *Phys. Rev. B* **59**, 1758–1775 (1999).
- 737 41. Blöchl, P. E. Projector augmented-wave method. *Phys. Rev. B* **50**, 17953–17979

- 738 (1994).
- 739 42. Mills, G., Jónsson, H. & Schenter, G. K. Reversible work transition state theory:  
740 Application to dissociative adsorption of hydrogen. *Surf. Sci.* **324**, 305-337 (1995).
- 741 43. Hjorth Larsen, A. *et al.* The atomic simulation environment—a Python library for  
742 working with atoms. *J. Phys. Condens. Matter* **29**, 273002 (2017).
- 743 44. Henkelman, G. & Jónsson, H. A dimer method for finding saddle points on high  
744 dimensional potential surfaces using only first derivatives. *J. Chem. Phys.* **111**,  
745 7010–7022 (1999).
- 746 45. Kästner, J. & Sherwood, P. Superlinearly converging dimer method for transition  
747 state search. *J. Chem. Phys.* **128**, 014106 (2008).
- 748 46. Thetford, A., Hutchings, G. J., Taylor, S. H. & Willock, D. J. The decomposition of  
749 H<sub>2</sub>O<sub>2</sub> over the components of Au/TiO<sub>2</sub> catalysts. *Proc. R. Soc. Math. Phys. Eng. Sci.*  
750 **467**, 1885–1899 (2011).
- 751
- 752

753 **Table 1** Catalytic performance of Au/ZSM-5 catalysts for the partial oxidation of methane.

Entry	Catalyst	Reactants CH <sub>4</sub> , O <sub>2</sub> , CO (bar) <sup>a</sup>	T (°C)	Time	Productivity (μmol/g <sub>cat</sub> )					Oxygenate Selectivity (%)	Oxygenate Productivity (μmol/g <sub>cat</sub> )
					Methanol	Methyl hydroperoxide	Acetic acid	Peracetic acid	CO <sub>2</sub>		
1	H-ZSM-5	20.7, 3.5, 0	240	2 h	1.18	0.38	2.62	0.68	2.34	77.7	4.86
2	Au/SiO <sub>2</sub>	20.7, 3.5, 0	240	2 h	0.10	0.04	0.78	0.18	1.44	58.9	1.10
3	Au/Al <sub>2</sub> O <sub>3</sub>	20.7, 3.5, 0	240	2 h	3.38	0.00	1.26	0.50	3.26	67.9	5.14
4	Au/ZSM-5	20.7, 3.5, 0	240	2 h	7.01	2.28	8.32	2.69	17.3	64.4	20.3
5	Au/ZSM-5	23.2, 1.0, 0	240	2 h	10.6	0.66	10.1	2.54	12.8	74.1	23.9
6	Au/ZSM-5	23.2, 1.0, 0	240	1 h	11.1	1.80	8.07	2.66	12.8	72.9	23.7
7	Au/ZSM-5	24.06, 0.14, 0	240	2 h	8.43	0.00	6.85	2.04	5.69	82.2	17.3
8	Au/ZSM-5- 0.25 <sup>b</sup>	24.06, 0.14, 0	240	2 h	5.70	1.74	4.11	1.36	b.d. <sup>c</sup>	100	12.9
9	Au/ZSM-5	20.7, 3.5, 0	240	5 min	3.34	0.00	3.79	0.70	1.42	89.7	7.83
10	Au/ZSM-5- 0.25 <sup>b</sup>	20.7, 3.5, 0	240	5 min	3.86	1.23	2.05	0.55	b.d. <sup>c</sup>	100	7.69 <sup>d</sup>
11	Au/ZSM-5	20.7, 1.0, 2.5	240	1 h	136	0.00	19.9	4.64	n.d. <sup>e</sup>	n.d. <sup>e</sup>	161
12	Au/ZSM-5	20.7, 1.0, 2.5	240	4 h	545	0.00	79.0	2.36	n.d. <sup>e</sup>	n.d. <sup>e</sup>	627

754 Reaction conditions: catalyst 0.5 wt.% Au/ZSM-5 (0.10 g), water (15 mL)

755 <sup>a</sup>Gas pressures measured at room temperature prior to reaction; <sup>b</sup>Au loading is 0.25 wt.%; <sup>c</sup>below detection limit; <sup>d</sup>7.3 mol/mol<sub>Au</sub>/h (37  
756 mmol/g<sub>Au</sub>/h) at 5 min reaction time, <sup>e</sup>not determined

757

758

## 759 **Figure Captions**

760

761 **Fig. 1 Catalytic performance of Au/ZSM-5 catalysts for methane oxidation. a-d,** The  
762 effect of O<sub>2</sub> partial pressure on the reaction at a total pressure of 24.2 bar (CH<sub>4</sub> + O<sub>2</sub>) and  
763 reaction time of 120 min. **e-h,** The effect of reaction time on the reaction with CH<sub>4</sub> (20.7 bar)  
764 and O<sub>2</sub> (3.5 bar). **a, e** 0.12 wt.% Au, **b, f** 0.25 wt.% Au, **c, g** 0.5 wt.% Au, and **d, h** 1.0 wt.%  
765 Au. For all the reactions: catalyst (0.1 g), 240 °C, H<sub>2</sub>O (15 mL).

766

767 **Fig. 2 Oxygenate selectivity as a function of methane conversion.** Reaction conditions  
768 (Supplementary Table 7): 0.5 wt.% Au/ZSM-5 catalyst (0.10 g), 240 °C, H<sub>2</sub>O (15 mL),  
769 methane reacted with air with total pressure 24.2 bar using nitrogen.

770

771 **Fig. 3 STEM-HAADF images of 0.5 wt.% Au/ZSM-5 catalysts. a, b,** fresh catalyst, and **c,**  
772 **d,** used catalyst after 2 h of methane oxidation reaction (23.2 bar CH<sub>4</sub>, 1.0 bar O<sub>2</sub>, 240 °C).

773

774 **Fig. 4 Calculated reaction pathways for methane activation by surface O atoms.** The  
775 zero of energy is for the clean surface, O<sub>2</sub>(g) and CH<sub>4</sub>(g) barrier heights are given in kJ mol<sup>-1</sup>  
776 with TS1 representing dissociation of O<sub>2</sub>(ads) and TS2 the activation of a methane H<sub>3</sub>C-H  
777 bond to form surface bound OH and CH<sub>3</sub> species. Energy values based on total calculated  
778 energy at PBE+D3 level without correction for vibrational contributions. Black lines are for  
779 the slab model of the Au(100) with (111) step edges, grey lines are for the Au<sub>38</sub> nanoparticle.  
780 Graphical images show the structures of TS2 with atom colours: Au; yellow, O; red, C; grey  
781 and H; white.

782

783 **Fig. 5 Yield of products as a function of time.** In all cases data for H<sub>2</sub>O solvent is shown  
784 with filled symbols and that for D<sub>2</sub>O solvent with open symbols. Dotted lines show least  
785 squares linear fits to the first 60 min of data with the initial gradient shown (s(H/D<sub>2</sub>O)) in  
786 units of μmol<sub>C</sub> g<sub>cat</sub><sup>-1</sup> min<sup>-1</sup> these slopes are proportional to the effective rate constants and so  
787 are used to calculate the k<sub>H</sub>/k<sub>D</sub> values discussed in the text. **a,** All products. **b,** Methanol yield.  
788 **c,** C<sub>2</sub> product yield. **d,** CO<sub>2</sub> yield. Reaction conditions: catalyst (0.1 g), H<sub>2</sub>O/D<sub>2</sub>O (15 mL),  
789 CH<sub>4</sub> (20.7 bar), O<sub>2</sub> (1.0 bar), N<sub>2</sub> (2.5 bar), 0.5 wt.% Au loading, reaction temperature  
790 (200 °C). All product yields are calculated as micromoles of carbon (μmol<sub>C</sub>).

791

792 **Fig. 6 Schematic illustration of the proposed surface catalysed reactions.** Blue arrows and  
793 lines are used for C<sub>1</sub> intermediates and products, red arrows and lines are used for C<sub>2</sub>  
794 intermediates and products. The phase of each product is indicated as (aq): aqueous or (aq/g):  
795 partitioned between aqueous and gas phase surface species are labelled with “\*”. The surface  
796 species in blue/red ellipses lead to observed partial oxidation  
797 products through hydrolysis or hydrogen transfer.

798

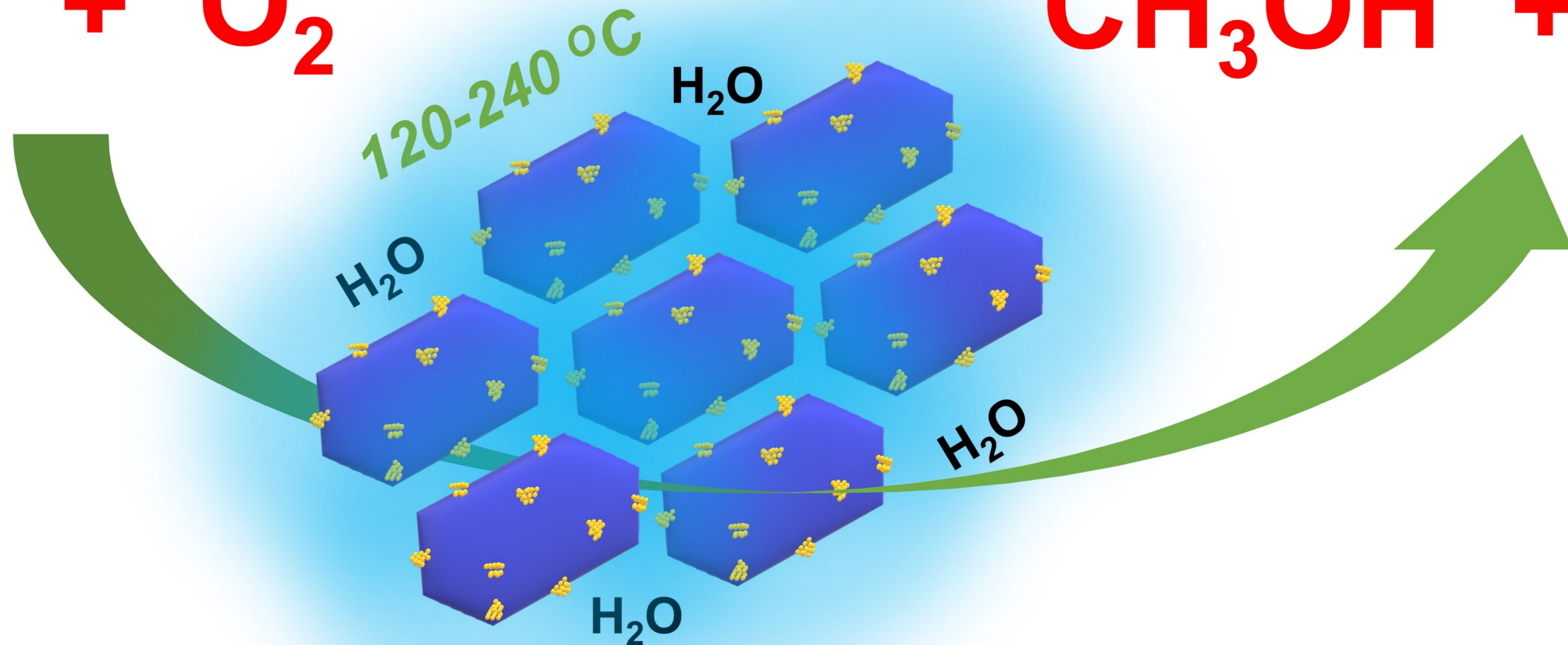
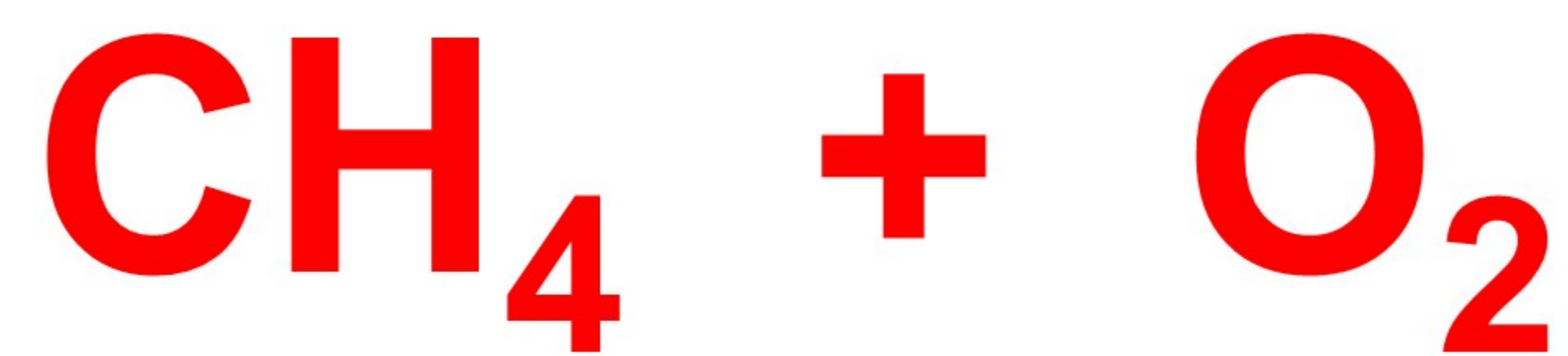
799

800

801

802

# Au/ZSM-5



▲ Liquid-phase oxygenates selectivity

$\text{CH}_3\text{C}(=\text{O})\text{OH}$ 
 $\text{CH}_3\text{C}(=\text{O})\text{OOH}$ 
 $\text{CH}_3\text{-OH}$ 
 $\text{CH}_3\text{-OOH}$ 
● Carbon dioxide

